Large-Eddy Simulation of Supercritical Hydrocarbon Flows in a Heated Horizontal Circular Tube

Shuto Yatsuyanagi[1] and Hideyuki Tanno[1]

Abstract

Large-eddy simulations of supercritical *n*-dodecane flow in a horizontal heated circular tube were conducted to clarify the hydrodynamic characteristics under supercritical pressure conditions. The fundamental equations were three-dimensional Navier-Stokes equations in general curvilinear coordinates, and to solve the compressible unsteady flows at low-Mach numbers accurately and effectively, a preconditioning method and a dual time-stepping technique were adopted for the system of equations. To observe the effects of pressure conditions, the hydrodynamic characteristics curves of *n*-dodecane were evaluated for three different outlet pressure conditions of 2.0, 2.5, and 6.0 MPa. The present large-eddy simulations demonstrate that the hydrodynamic characteristics are expressed as cubic curves at 2.0 and 2.5 MPa conditions. The present findings suggest that Ledinegg instability can occur in supercritical *n*-dodecane flow in a heated horizontal circular tube. The evaluation of the local Nusselt number and flow visualization analysis revealed that the enhanced ejection motion associated with large density fluctuations transports the low-density fluid near the heated wall toward the mainstream, reducing bulk density and significantly accelerating the flow. Eventually, it was found that the multi-valued hydrodynamic characteristic curve is formed due to the significant increase of acceleration pressure drop under supercritical pressure conditions.

Keywords: *Regenerative cooling, Large-Eddy Simulation, Ledinegg instability, Hydrodynamic characteristics, Supercritical pressure*

Nomenclature

Latin

E – total internal energy
G – mass flow rate
H – total enthalpy
h – enthalpy
J – Jacobian of transformation
q – heat flux
p – pressure
T – temperature
t – time
$U_i\ (i = 1, 2, 3)$ – contravariant velocities
$u_i\ (i = 1, 2, 3)$ – velocities
$x_i\ (i = 1, 2, 3)$ – Cartesian coordinates
p – pressure drop in a heated tube

Greek

θ – preconditioning parameter
κ – thermal conductivity
μ – molecular viscosity
$\xi_i\ (i = 1, 2, 3)$ – general curvilinear coordinates
ρ – density
$\tau_{ij}\ (i, j = 1, 2, 3)$ – viscous stress tensors

Subscripts

c – critical point
cs – cross-section
in – inlet
out – outlet
pc – pseudocritical
w – wall

[1] *JAXA (Japan Aerospace Exploration Agency), Kakuda Space Center, Research and Development Directorate, Research Unit IV, 1-Koganesawa, Kimigaya, Kakuda, Miyagi, yatsuyanagi.shuto@jaxa.jp*

1. Introduction

Flow instability is a crucial issue in the design and operation of industrial systems such as steam generators, boiling water reactors, and high-power-density boilers. The work on flow instability was started by Ledinegg [1], who demonstrated that the pressure drop in a heated channel is expressed as a cubic curve for the flow rate. This relationship is well-known as the multi-valued hydrodynamic characteristic curve. The negative slope region in the hydrodynamic characteristic curve has been recognized as a cause of flow excursion, which is one of the static instabilities. In addition, the flow excursion studied by Ledinegg is often called the Ledinegg instability. After Ledinegg's research [1] on flow instability, a great deal of experimental and numerical data [2-4] has been accumulated to the present. While much of previous studies focus on the two-phase flow instabilities under subcritical pressure, the flow instabilities under supercritical pressure have recently attracted the attention of researchers as the industrial use of supercritical fluids has expanded. In particular, the flow instabilities of supercritical hydrocarbon in the regenerative cooling system have been a barrier to the development of an engine of hypersonic aerospace vehicle such as a Rocket-Based Combined Cycle engine [5]. Flow instabilities can disturb heat transfer and induce mechanical vibration, and in extreme situations, possibly cause even mechanical breakdown.

Although many studies have been conducted on flow instability, studies on flow instability of hydrocarbon fuels are still rare compared to those of water, CO2, and refrigerants. The flow instability of the hydrocarbon at supercritical pressure is one of the key issues in terms of the development of a regenerative cooling system. Hitch and Karpuk [6] were experimentally investigated and reported the flow instabilities of methylcyclohexane and JP-7 near the pseudocritical temperature and demonstrated that no substantial improvements by flow instabilities in heat transfer coefficients were realized for normally forced convection. Wang et al. [7] experimentally investigated the thermo-acoustic instability of RP-3 in mini-tubes under a supercritical pressure condition and employed two dimensionless parameters of the true trans-pseudocritical number and the sub-pseudocritical number [8] to evaluate stability boundaries. Zhou et al. [9] experimentally studied the pressure-drop type instability of *n*-dodecane in a system with a horizontal circular tube and accumulator, and the mechanism of instability that occurs in pseudocritical temperature region and in pyrolysis temperature region was investigated using a zero-dimensional homogeneous model. Yang et al. [10] experimentally demonstrated the multi-valued hydrodynamic characteristic curve of supercritical cyclohexane, which suggests the occurrence of Ledinegg instability under supercritical pressure conditions. However, researchers differ on the presence of multi-valued hydrodynamic characteristics (i.e., the presence of Ledinegg instability) at supercritical pressures [10], and no consensus has been reached yet. Toward the prediction of the Ledinegg instability, the formation mechanisms of multivalued hydrodynamic characteristic curves must be elucidated enough.

In the present study, we investigated the formation mechanisms of the multi-valued hydrodynamic characteristic curves using the large eddy simulation (LES) code. To validate the numerical method of LES, the flows in a horizontal unheated circular tube were simulated. The simulated adiabatic friction coefficients were compared with theoretical values and previous correlations to prove that the present LES has sufficient capability to predict the pressure field. Eventually, the LES were conducted for *n*-dodecane flows in a horizontal heated circular tube at supercritical pressure. Hydrodynamic characteristic curves were obtained under different three supercritical pressure conditions. To clarify the generation mechanisms of pressure drop behind the formation of the hydrodynamic characteristic curves, the present LES analyzed the flow properties, such as the thermodynamic properties and local Nusselt number, and turbulence statistics in the horizontal heated circular tube.

2. Numerical methods

2.1. Fundamental equations

The fundamental equations consist of the conservation equations of mass, momentum, and total energy. The set of equations is expressed in the system of equations in the three-dimensional general curvilinear coordinates. To solve the compressible unsteady flows at low-Mach numbers accurately and effectively, a preconditioning method and a dual time-stepping technique [11] are adopted for the system of equations. The preconditioning technique has been used in the context of LES for low-Mach number flows [12-14]. The system of equations is written in the vector form as follows:

$$\frac{\partial \boldsymbol{Q}}{\partial t} + \boldsymbol{\Gamma}\frac{\partial \widehat{\boldsymbol{Q}}}{\partial \tau} + \frac{\partial \boldsymbol{F}_i}{\partial \xi_i} + \frac{\partial \boldsymbol{F}_{vi}}{\partial \xi_i} = 0 \quad (i = 1, 2, 3), \tag{1}$$

where

$$\boldsymbol{Q} = J \begin{bmatrix} \rho \\ \rho u_1 \\ \rho u_2 \\ \rho u_3 \\ E \end{bmatrix}, \widehat{\boldsymbol{Q}} = J \begin{bmatrix} p \\ u_1 \\ u_2 \\ u_3 \\ T \end{bmatrix}, \boldsymbol{F}_i = J \begin{bmatrix} \rho U_i \\ \rho u_1 U_i + \dfrac{\partial \xi_i}{\partial x_1}p \\ \rho u_2 U_i + \dfrac{\partial \xi_i}{\partial x_2}p \\ \rho u_3 U_i + \dfrac{\partial \xi_i}{\partial x_3}p \\ (E+p)U_i \end{bmatrix}, \boldsymbol{F}_{vi} = J\frac{\partial \xi_i}{\partial x_j}\begin{bmatrix} 0 \\ \tau_{j1} \\ \tau_{j2} \\ \tau_{j3} \\ \tau_{jk}u_k + \kappa\dfrac{\partial T}{\partial x_j} \end{bmatrix}.$$

$\boldsymbol{Q}$, $\widehat{\boldsymbol{Q}}$, $\boldsymbol{F}_i$, and $\boldsymbol{F}_{vi}$ are the vectors of the conservative variables, primitive variables, inviscid flux, and viscous flux, respectively. $\boldsymbol{\Gamma}$ is the preconditioning matrix derived from the Jacobian matrix for $\widehat{\boldsymbol{Q}}$. As $\tau \to \infty$, the pseudo-time term in Eq. (1) converges to zero and the equation becomes the conservative system.

2.2. Numerical schemes

The present LES employed a preconditioning LU-SGS scheme [15] for the time integration of pseudo time and a second-order three-point backward difference scheme for the time integration of physical time. The numerical flux was evaluated by using the preconditioning flux-vector splitting scheme [15]. The fifth-order alternative weighted essentially non-oscillatory scheme [16] was applied for higher-order accuracy. The double-flux model in the preconditioning method [17] was employed to eliminate the spurious oscillations caused by the drastic thermophysical properties change. The viscous flux was evaluated by a tridiagonal sixth-order compact difference scheme [18]. In the present study, an implicit LES was conducted, and the effects of sub-grid scale turbulence were implicitly considered by the inherent numerical dissipation of the numerical scheme.

2.3. Thermophysical property models

Thermodynamic properties of n-dodecane were calculated using the Helmholtz free-energy EoS proposed by Lemmon and Huber [19], and the transport property for n-dodecane were given by using the correlations proposed by Huber et al. [20]. These EoS and correlation are defined in the REFPROP [21]. A look-up table method was used to reduce the calculation cost of thermophysical properties. The data points of look-up tables in the pressure and temperature parameter space were set with a constant interval of $\Delta p = 0.005 \text{ MPa}$ and $\Delta T = 0.75 \text{ K}$. The thermophysical properties required by the flow simulation are calculated by linear interpolation of the values in the prepared lookup table.

3. LES of n-dodecane flows in a horizontal unheated circular tube

Fig. 1 shows the schematic of the present LES for horizontal circular tube flows. The r, θ, and z directions correspond to radial, circumferential, and axial directions. A radial, circumferential, and axial velocity were expressed as u_r, u_θ, and u_z, respectively. The computational domain consisted of an inflow generator and a test section. The length of the inflow generator and the test section were $L/D = 20$ and $L/D = 250$. Here, the tube diameter was $D = 1 \text{ mm}$. The additional buffer region was placed at the outlet of the test section to remove the outlet boundary reflections. The periodic boundary condition was applied to the streamwise direction in the inflow generator to generate a fully developed turbulent velocity profile for the inlet boundary of the test section. The inlet temperature and outlet pressure were specified. The outlet pressure was set to 2.0 MPa in all cases. The wall heat flux was $q_{\text{w}} = 0$, i.e., an adiabatic wall condition, in this section. The present simulations considered the inlet Reynolds number conditions $220 \le Re \le 44500$. Here, $Re = \rho_{\text{in}}u_{\text{in}}D/\mu_{\text{in}}$. Nonslip and adiabatic boundary conditions were imposed on the r-minimum wall. Table 1 shows the different three grid systems used in the present LES. Here, the dimensional wall spacings were set to $\Delta r_{\text{w}} = 0.001 \text{ mm}$ in all grid systems. The nondimensional physical time step was set to $dt = 4.0 \times 10^{-2}$. The CFL number of the pseudo time was set to 4.0, however the value of $\delta\tau/\delta t$ was limited to less than unity for stability. Iterative calculations were continued until the residue (L2 norm) decreased by 2 orders of magnitude.
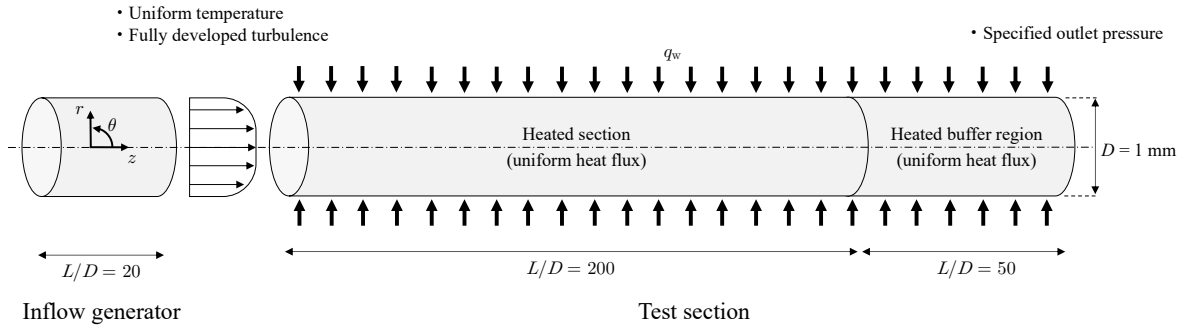
Fig 1. Schematic of the present LES for horizontal circular tube flows.

Table 1. Computational grid for horizontal circular tube flows under unheated condition

Grid	Inflow generator			Test section		
	N_r	N_θ	N_z	N_r	N_θ	N_z
Fine	91	241	151	91	241	1561
Medium	61	161	101	61	161	1041
Coarse	31	81	51	31	81	521

Fig. 2 shows the adiabatic friction factors to the Reynolds number for the different three grid systems. The solid and dashed lines indicate the friction factor of laminar flow $f = 64/Re$ and the Filonenko correlation, respectively. In the laminar region, all grids agreed with the theoretical values, and grid convergence was good. In the turbulent region, although the coarse grid underestimated the Filonenko correlation at high Reynolds number conditions $Re > 10000$, the medium and fine grids were in good agreement with the Filonenko correlation and clearly showed the grid convergence. The results demonstrated enough capability of the present LES to reproduce the pressure drop in a horizontal circular tube. In the following section, the medium grid was used to conduct the LES for n-dodecane flows.
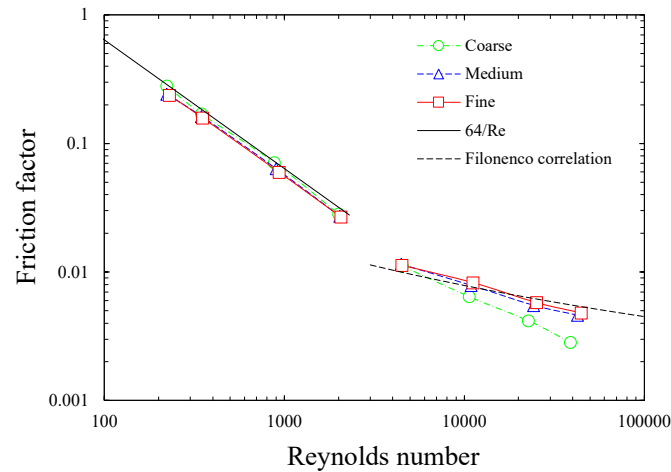

Fig 2. Adiabatic friction factors to the Reynolds number for the different three grid systems.

4. LES of n-dodecane flows in a horizontal heated circular tube

The computational target was the same in Fig. 1. Table 2 shows the computational conditions of the present LES for n-dodecane flows. The inlet temperature was set to 500 K, where n-dodecane is in the liquid state. The heat flux of 600 kW/m^2 was applied to the wall boundary conditions. The different three outlet pressure conditions of 2.0, 2.5, and 6.0 MPa, which are above the critical pressure of 1.82 MPa, were considered in the present LES. The LES were conducted on several mass flow rate conditions between 0.5 and 4.0 g/s. The inlet Reynolds numbers in these pressure and mass flow rate conditions were $3102 \leq Re \leq 27055$.

Fig. 3 shows the hydrodynamic characteristic curves for the mass flow rate for different three pressure conditions. The hydrodynamic characteristic curve at $p = 2.0 \text{ MPa}$ has a clear negative slope from 1.25 g/s to 2.0 g/s. On the one hand, the negative slope at $p = 2.5 \text{ MPa}$ exists only in the narrow region from 1.25 g/s to 1.50 g/s, and it no longer exists at 6.0 MPa. The negative slope region in the hydrodynamic characteristic curve has been well-known as a cause of flow excursion, which is one of the static instabilities. Fig. 3 demonstrates the possibility of flow instability at $p = 2.0 \text{ MPa}$ and 2.5 MPa. The points A in Fig. 3 indicate minimum points of hydrodynamic characteristic curves. In the case of $p = 2 \text{ MPa}$, the outlet bulk temperature at the minimum points was $T_{out} = 652 \text{ K}$ ($T_{out}/T_{pc} = 0.98$), and the streamwise averaged wall temperature was $T_{\text{w}} = 749 \text{ K}$ ($T_{\text{w}}/T_{\text{pc}} = 1.13$). Yang et al. [10] also experimentally demonstrated the relationship of $T_{out} < T_{pc} < T_w$ at the minimum point. In addition, Fig. 3 exhibits the dependence of pressure drop on outlet pressure conditions, and the pressure drop significantly increased with approaching the critical pressure. The trend was also reported by Yang et al. [10]. In the following, the transcritical hydrocarbon flows at $p = 2 \text{ MPa}$ and 6 MPa will be compared under the mass flow rate condition of $G = 1.75 \text{ g/s}$ to clarify the generation mechanisms of pressure drop behind the formation of the multi-valued hydrodynamic characteristic curves in a heated circular tube.

Table 2. Computational conditions of the present LES

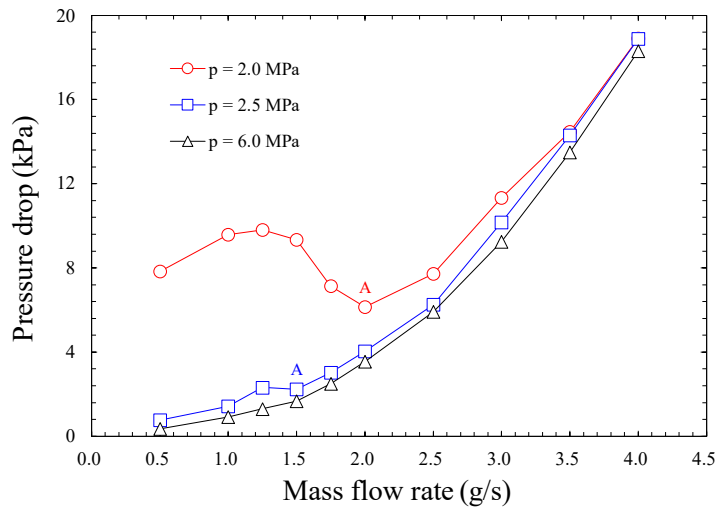| Fluid	Inlet temperature (K)	Heat flux (kW/m^2)	Outlet pressure (MPa)	Mass flow rate (g/s)
N-dodecane	500	600	2.0, 2.5, 6.0	0.5-4.0

Fig 3. Hydrodynamic characteristic curves for three different outlet pressure conditions.

Fig. 4 shows profiles of mean temperature, density, viscosity, and thermal diffusivity in the radial direction for different two pressure conditions. The fluid temperature rises toward the outlet by heating from the wall surface at $r/D = 0.5$. The wall temperatures at $z/D = 100$ and 200 exceed the pseudocritical temperature in all outlet pressure conditions. Focusing on the temperature profile at $z/D = 200$, the thermal boundary layer at $p = 2 \text{ MPa}$ is thicker than that at $p = 6 \text{ MPa}$ which is related to the transcritical turbulent transportation as will be discussed later. When crossing the pseudocritical temperature, the density and viscosity decrease, and the thermal diffusivity drastically increases. The change in thermophysical properties at $p = 2 \text{ MPa}$ is significant because of the strong real-gas effects. The minimum density at $p = 2 \text{ MPa}$ and 6 MPa are $\overline{\rho}/\rho_0 = 0.12$ and 0.40, respectively. The minimum viscosity at $p = 2 \text{ MPa}$ and 6 MPa are $\overline{\mu}/\mu_0 = 0.07$ and 0.12, and the pressure dependence of viscosity in the supercritical state is small compared to that of density. The thermal diffusivity at $p = 2 \text{ MPa}$ and 6 MPa achieve $\overline{\alpha}/\alpha_0 = 4.58$ and 1.69 at the heated wall. Therefore, the thermal diffusion related to the heat conduction is enhanced near the heated wall at $p = 2 \text{ MPa}$.

(a) temperature

(b) density
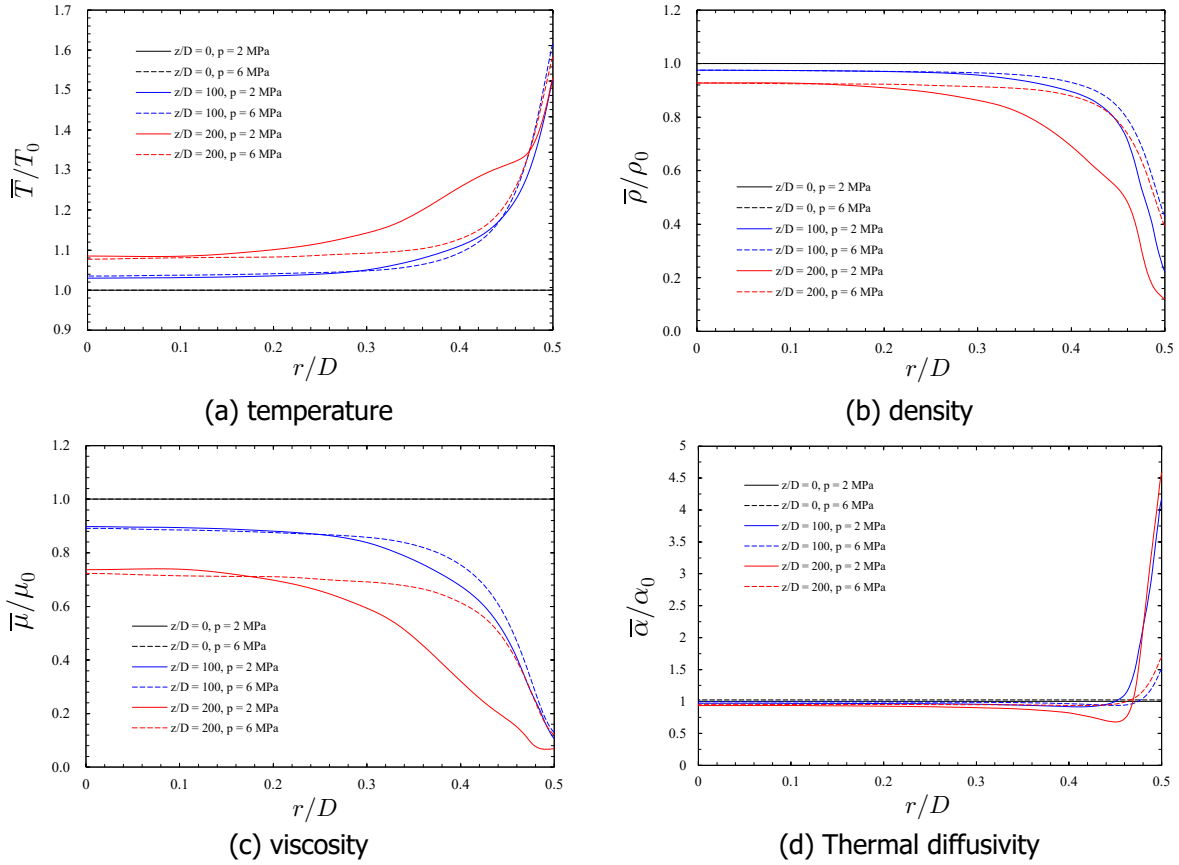
(c) viscosity

(d) Thermal diffusivity

Fig 4. Profiles of mean temperature, density, viscosity, and Prandtl number in the radial direction for different two outlet pressure conditions at $G = 1.75 \text{ g/s}$.

Fig. 5 shows profiles of Reynolds- and Favre-averaged streamwise velocity in the radial direction for different two pressure conditions. The streamwise velocity is nondimensionalized by the mainstream velocity at the inlet. The flow acceleration in the streamwise direction was observed at $p = 2 \text{ MPa}$, and the streamwise velocity in the mainstream increases by 1.6 times from inlet to outlet. On the one hand, the streamwise velocity at $p = 6 \text{ MPa}$ accelerates only near the heated wall. There is little acceleration in the mainstream.

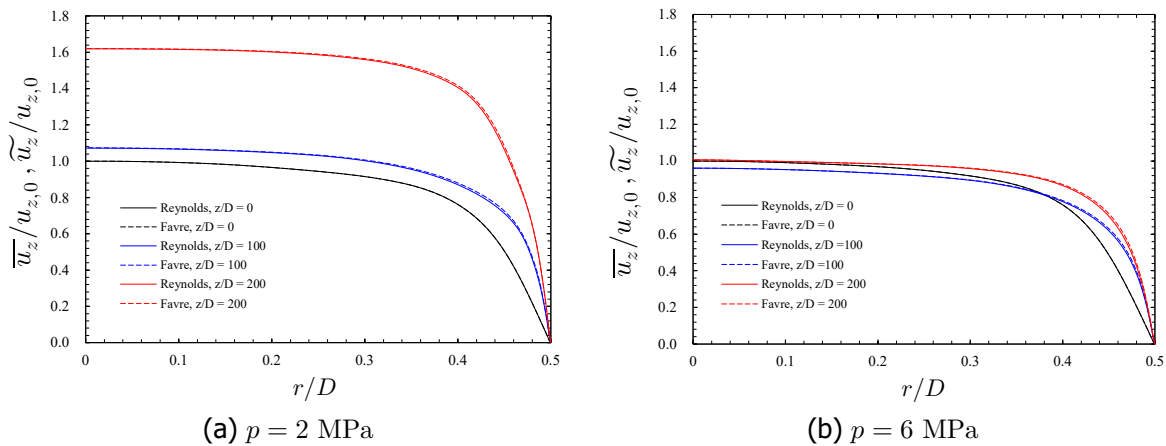(a) $p = 2 \text{ MPa}$

(b) $p = 6 \text{ MPa}$

Fig 5. Profiles of Reynolds- and Favre-averaged streamwise velocity in the radial direction for different two outlet pressure conditions at $G = 1.75 \text{ g/s}$.

Fig. 6 shows profiles of Reynolds- and Favre-averaged radial velocity in the radial direction for different two pressure conditions. Focusing on the difference in the streamwise direction, the radial velocity decreased toward the outlet and finally became negative in the wide region. Note that the negative radial velocity is the flow from the wall toward the mainstream. The formation of negative radial velocity was pronounced at $p = 2$ MPa and especially near the heated wall. The mechanisms of the formation of negative radial velocity will be discussed later.
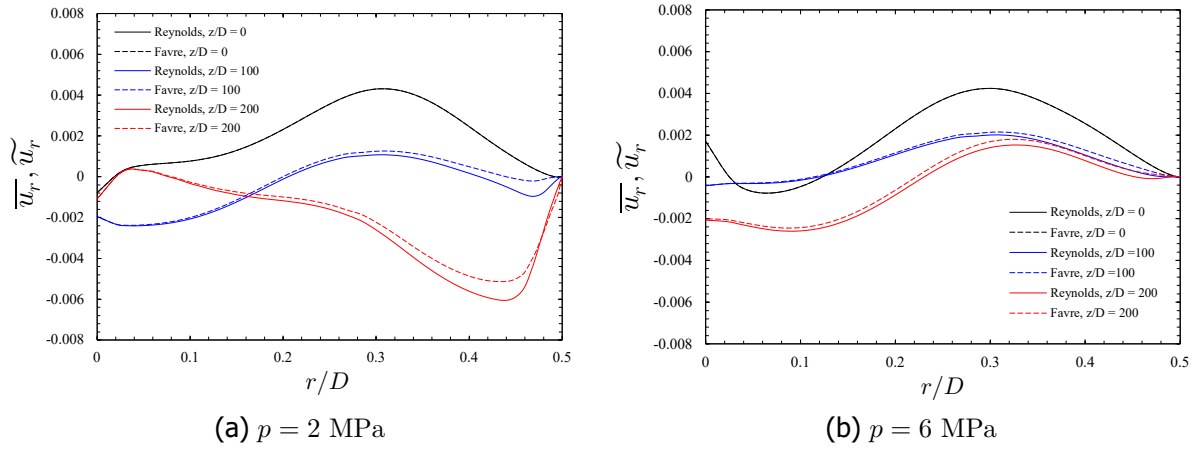

(a) $p = 2$ MPa   (b) $p = 6$ MPa

Fig 6. Profiles of Reynolds- and Favre-averaged radial velocity in the radial direction for different two outlet pressure conditions at $G = 1.75$ g/s.

Fig. 7 shows profiles of spatial-averaged mean viscous shear stress in the radial direction for different two outlet pressure conditions. The absolute value of the viscous shear stress reduces toward the outlet and the heated wall because the viscosity decreases as shown in Fig. 4. The wall shear stress at $p = 2$ MPa is slightly smaller than that at $p = 6$ MPa.
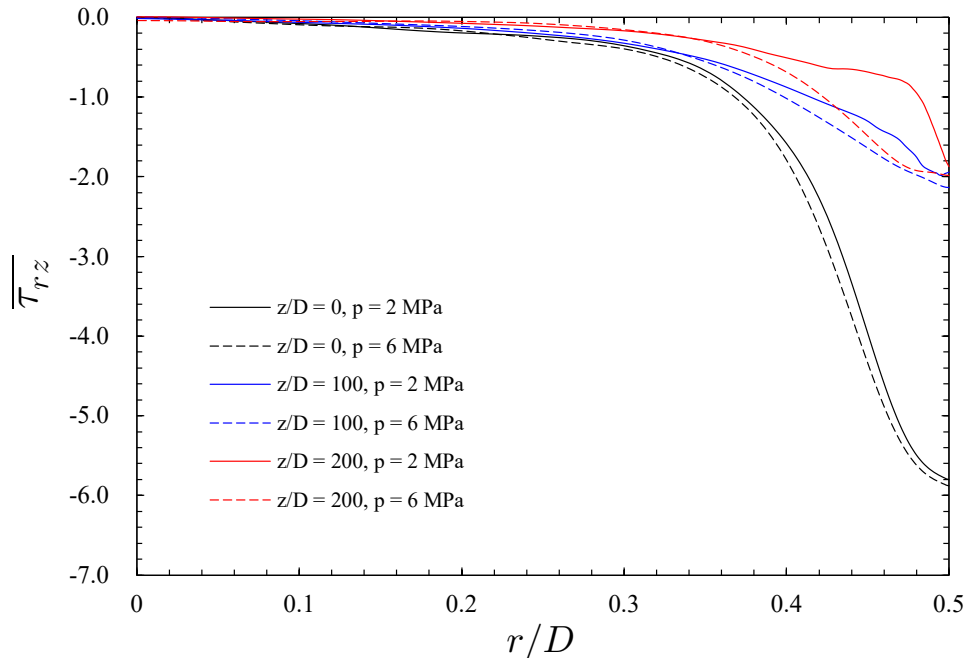

Fig 7. Profiles of spatial-averaged mean viscous shear stress in the radial direction for different two outlet pressure conditions at $G = 1.75\ g/s$.

Fig. 8 shows profiles of density variances in the radial direction for different two outlet pressure conditions. The maximum density variances show near the heated wall. The fluid density changes drastically across the pseudo-critical temperature near the heated wall as shown in Fig. 4. The large density fluctuation is caused by the drastic density change in a narrow temperature range, which is the unique behavior of the transcritical flow. As shown in Fig. 8, density variances are larger for conditions closer to the critical pressure. For example, the maximum density variance at $p = 2$ MPa is greater than unity, while that at $p = 6$ MPa is 0.3.
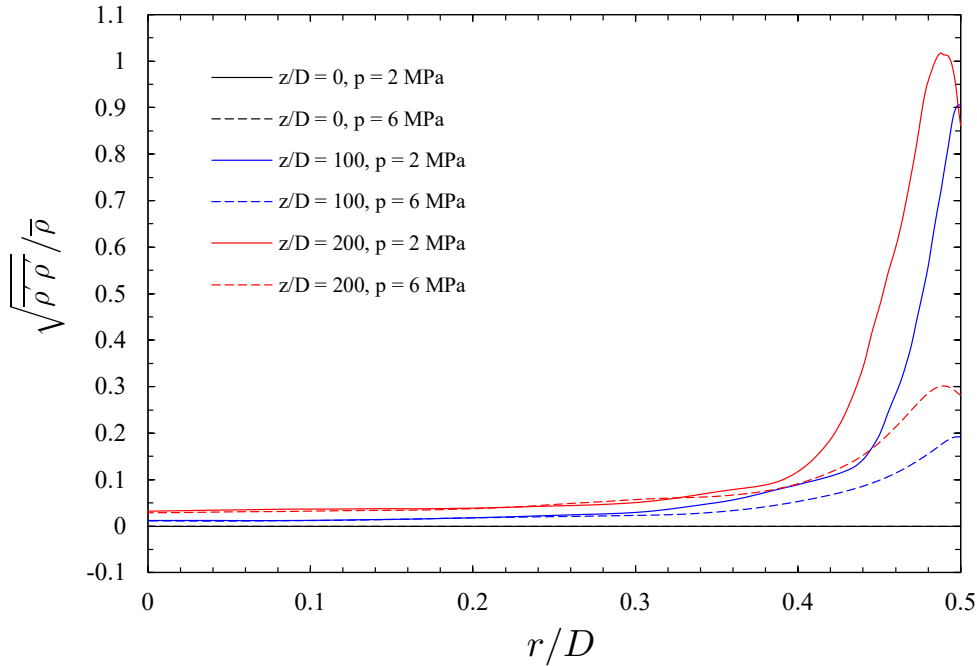
Fig 8. Profiles of density variances in the radial direction for different two outlet pressure conditions at $G = 1.75$ g/s.

Fig. 9 shows profiles of Favre-averaged streamwise and wall-normal velocity fluctuations in the radial direction for different two outlet pressure conditions. The velocity fluctuation profiles in the radial direction have $\overline{u_z''} < 0$ and $\overline{u_r''} < 0$. Therefore, the ejection motion ($\overline{u_z''} < 0$ and $\overline{u_r''} < 0$) was dominant in the transcritical flows in the heated circular tube. The previous DNS [22] demonstrated the enhancement of the ejection motion in a transcritical turbulent boundary layer. The ejection motion is enhanced toward the outlet at both pressure conditions, and with more intense ejection at $p = 2$ MPa.
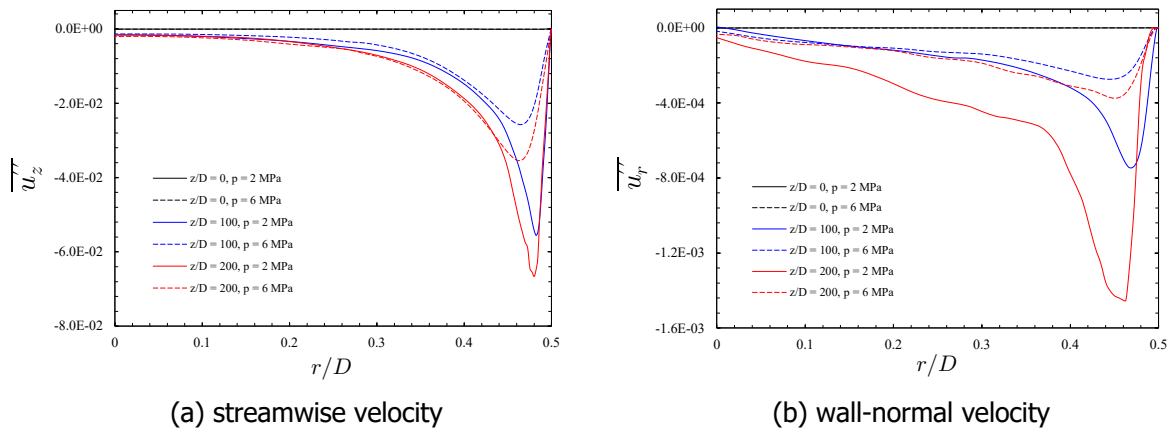
(a) streamwise velocity

(b) wall-normal velocity

Fig 9. Profiles of Favre-averaged streamwise and wall-normal velocity fluctuations in the radial direction for different two outlet pressure conditions at $G = 1.75$ g/s.

These results can be explained by the following definitions for Favre-averaged velocity fluctuations

$$\overline{u_i''} = \overline{u_i - \widetilde{u_i}} = \overline{u_i} - \frac{\overline{(\overline{\rho} + \rho')(\overline{u_i} + u_i')}}{\overline{\rho}} = -\frac{\overline{\rho' u_i'}}{\overline{\rho}}. \tag{2}$$

Eq. (2) shows that the Favre-averaged velocity fluctuations are enhanced by the density fluctuation. In the present case, the density fluctuation increases near the pseudo-critical temperature as shown in Fig. 8, and hence the Favre-averaged velocity fluctuations related to the ejection motion ($\overline{u_z''} < 0$ and $\overline{u_r''} < 0$) are enhanced. The enhancement of ejection motion associated with density fluctuations provides a certain explanation for the development of negative radial velocity in the streamwise direction shown in Fig. 6. The reasons for $\overline{u_z''} < 0$ and $\overline{u_r''} < 0$, i.e., $-\overline{\rho' u_z'} < 0$ and $-\overline{\rho' u_r'} < 0$, will be discussed later with results of flow visualization.

In the following, the mechanism of the increase in pressure drop approaching the critical pressure shown in Fig. 3 will be further discussed. The pressure drop can be decomposed into the following three contributions: acceleration pressure-drop Δp_a, frictional pressure-drop Δp_f and gravitational pressure drop Δp_g. Since the present LES had $Ri \leq 5 \times 10^{-3}$, the gravitational pressure drop can be neglected. Therefore, the total pressure drop Δp is expressed as follow:

$$\Delta p = \Delta p_a + \Delta p_f + \Delta p_g \approx \Delta p_a + \Delta p_f \tag{3}$$

Further, in the present study, the acceleration pressure-drop and the frictional pressure drop are evaluated by the following relations:

$$\Delta p_a = (\rho_b u_b^2)_{\text{out}} - (\rho_b u_b^2)_{\text{in}}, \tag{4a}$$

$$\Delta p_f = \frac{4L\overline{\tau_w}}{D}. \tag{4b}$$

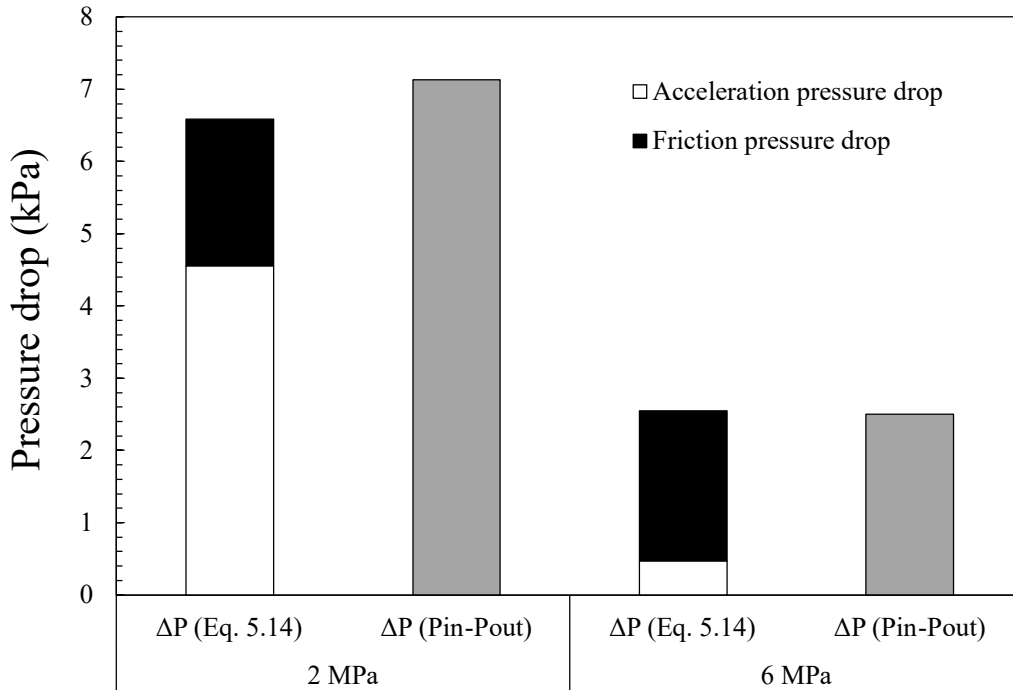Where L is tube length, τ_w is wall shear stress, and D is the tube diameter. Fig. 10 shows the comparison of the pressure drop evaluated by Eq. (3) and the total pressure drop $\Delta p = p_{in} - p_{out}$ for different two outlet pressure conditions. The errors for the total pressure drop at $p = 2 \text{ MPa}$ and at

Fig 10. Comparison of the pressure drop evaluated by Eq. (3) and the total pressure drop $\Delta p = p_{\text{in}} - p_{\text{out}}$ for different two outlet pressure conditions at $G = 1.75 \text{ g/s}$.

6 MPa were 7.6% and 1.9%, respectively. Fig. 10 shows the strong pressure dependence of acceleration pressure drop. Although the frictional pressure drop was slightly lower at $p = 2$ MPa, the difference due to the pressure condition is relatively small. Note that the decrease in the frictional acceleration pressure drop at $p = 2$ MPa was caused by the decrease in bulk density. Two factors cause pressure drop approaching the critical pressure was also reported in the existing study [23]. Eventually, it was clarified the increase in acceleration pressure drop at $p = 2$ MPa caused the formation of a negative slope region in the hydrodynamic characteristic curve. From Eq. (4a), the increase in the the decrease in bulk density at $p = 2$ MPa. The first factor is that the density in the supercritical state at $p = 2$ MPa is lower than that at $p = 6$ MPa as shown in Fig. 4(b). Therefore, the fluid density in the heated tube at $p = 2$ MPa significantly decreases because of thermal expansion. The second factor is that the low-density region has expanded to the mainstream region due to the heat transfer enhancement and the expansion of the temperature boundary layer at $p = 2$ MPa as shown in Fig. 4(a). In the following, we focus on the mechanisms of heat transfer enhancement directly related to the increase in the acceleration pressure drop at $p = 2$ MPa. To clarify the heat transfer enhancement in the transcritical flow, the local Nusselt number at $z/D = 200$ is evaluated for both outlet pressure conditions of $p = 2$ MPa and 6 MPa.

Fukagata et al. [24] proposed the Fukagata, Iwamoto, and Kasagi (FIK) identity which can express the individual contribution to the frictional pressure drop. The FIK identity has been extended to the Nusselt number. From now on, the FIK identity has been applied to several types of flows such as fully developed channel and pipe flows [25], compressible turbulent channel flows [26], developing turbulent boundary layers [27], heated developing turbulent boundary layers [28], strong heated air flows [29], supercritical fluid flows [30]. An expression for the FIK identity for the Nusselt number is obtained by double integrating the Favre-averaged energy equation. The FIK identity for the Nusselt number derived by Zhao et al. [30] is as follows: where the first term $N1$ in the right-hand side is the laminar contribution, the second term $N2$ is the turbulent contribution, and the other terms $N3 - N8$ are inhomogeneous contributions.

$$
\begin{aligned}
Nu_{FIK} = &\underbrace{\frac{8}{k_b(T_w - T_b)} \int_0^1 r \overline{\alpha} \frac{\partial \overline{h}}{\partial r} r dr}_{N1} - \underbrace{\frac{8 Re_{b0} Pr_0}{k_b(T_w - T_b)} \int_0^1 \overline{r \rho h'' u_r''} r dr}_{N2} \\
&\underbrace{- \frac{4 Re_{b0} Pr_0}{k_b(T_w - T_b)} \int_0^1 (1 - r^2) \left\langle \frac{1}{r} \frac{\partial r \overline{\rho} \widetilde{h} \widetilde{u_r}}{\partial r} \right\rangle r dr}_{N3} \\
&\underbrace{- \frac{4 Re_{b0} Pr_0}{k_b(T_w - T_b)} \int_0^1 (1 - r^2) \left\langle \frac{\partial \overline{\rho} \widetilde{h} \widetilde{u_z}}{\partial z} \right\rangle r dr}_{N4} \\
&\underbrace{- \frac{4 Re_{b0} Pr_0}{k_b(T_w - T_b)} \int_0^1 (1 - r^2) \left\langle \frac{\partial \overline{\rho h'' u_z''}}{\partial z} \right\rangle r dr}_{N5} \\
&\underbrace{+ \frac{4}{k_b(T_w - T_b)} \int_0^1 (1 - r^2) \left\langle \frac{1}{r} \frac{\partial}{\partial r} \left(\overline{r \alpha' \frac{\partial h'}{\partial r}} \right) \right\rangle r dr}_{N6} \\
&\underbrace{+ \frac{4}{k_b(T_w - T_b)} \int_0^1 (1 - r^2) \left\langle \frac{\partial}{\partial z} \left(\overline{\alpha} \frac{\partial \overline{h}}{\partial z} \right) \right\rangle r dr}_{N7} \\
&\underbrace{+ \frac{4}{k_b(T_w - T_b)} \int_0^1 (1 - r^2) \left\langle \frac{\partial}{\partial z} \left(\overline{\alpha' \frac{\partial h'}{\partial z}} \right) \right\rangle r dr}_{N8}
\end{aligned}
\tag{5}
$$

Fig. 11 shows the local Nusselt numbers calculated by Eq. (5) at $z/D = 200$ for different two outlet pressure conditions. The $N6$, $N7$, and $N8$ terms are not shown here because they are negligibly small in the present case. The total Nusselt numbers of $p = 2$ MPa and 6 MPa calculated by Eq. (5) were $Nu_{FIK} = 68$ and 38, respectively. The Nusselt numbers of $p = 2$ MPa and 6 MPa calculated by the

original definition of $Nu = q_w D/k_b(T_w - T_b)$ were $Nu = 40$ and 28, respectively. Although the FIK identity slightly overestimated the Nusselt numbers calculated by the original definition, the trend for pressure conditions was reproduced. Focusing on the $N1$ term, that at $p = 2$ MPa was larger because the thermal diffusivity greatly increases as shown in Fig. 4(d). Differences depending on pressure conditions in the $N2$ and $N5$ terms were relatively small and were less than 1%. The differences depending on pressure conditions were seen in $N3$ and $N4$. In the present case, the strong ejection motion induces negative radial velocities as shown in Fig. 6(a), thus $\partial \widetilde{u_r}/\partial r$, which is the component of $N3$, is negative in most regions. As a result, the $N3$ term had a major and positive contribution at $p = 2$ MPa. On the one hand, $N4$ term had a large negative contribution. Note that the negative contribution of $N4$ is intensified at $p = 2$ MPa whereas the positive contribution of $N3$ increases. As already discussed, the radial transport of the low-density fluid near the heated wall to the mainstream by vigorous ejection motion leads to a decrease in bulk density and a significant flow acceleration. The flow acceleration increases the $\partial \widetilde{u_z}/\partial z$, which is the components of $N4$, resulting in the negative contribution of $N4$ being intensified. The series of heat transfer enhancement/deterioration mechanisms related to $N3$ and $N4$ were not found at $p = 6$ MPa, and the dominant in the heat transfer at $p = 6$ MPa was the turbulent contribution term of $N2$.
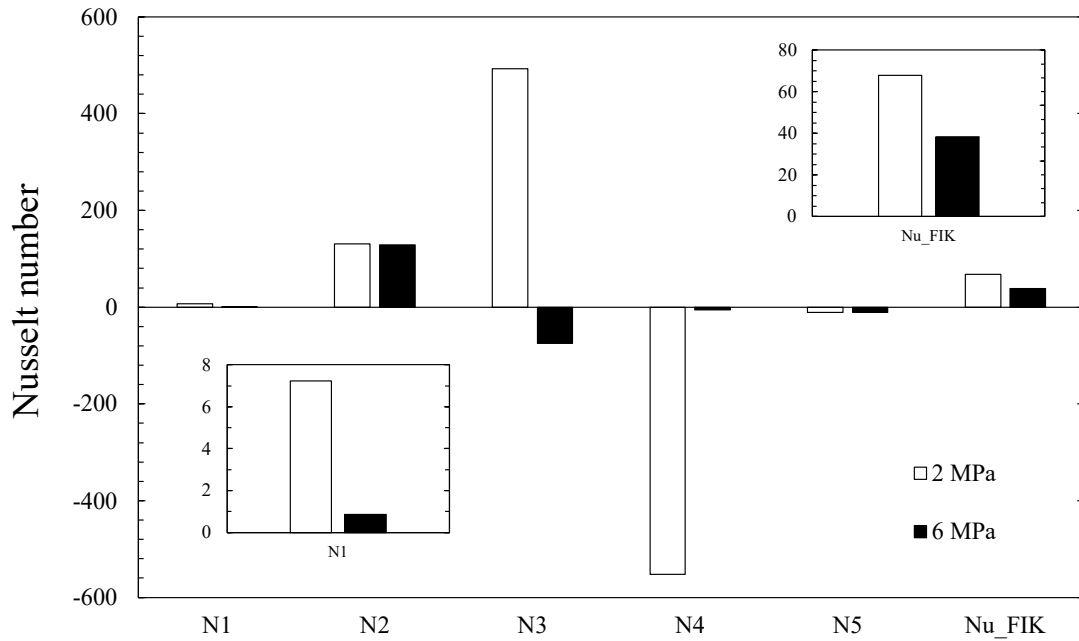

Fig 11. Local Nusselt numbers calculated by the FIK identity at $z/D = 200$ for different two outlet pressure conditions at $G = 1.75$ g/s.

To investigate the flow phenomenon in the negative slope region, Fig. 12 visualizes instantaneous snapshots for the temperature, isobaric-specific heat, and streamwise velocity in the cross-section at $z/D = 180$ under the computational conditions of $G = 1.75$ g/s and $p = 2.0$ MPa. The black and white contour lines indicate the c_p filaments of 5000 and 10000 J/kg/K, respectively. Instantaneous cross-stream velocity vectors are superimposed on the Fig. 12(c). Whereas the fluid temperature in the mainstream region was around $T = 570$ K, which is in the liquid state of n-dodecane, it raised to $T = 840$ K by constant heat flux from the heated wall. The temperature varied in the cross-section through the pseudocritical temperature of $T_{pc} = 665$ K at $p = 2.0$ MPa. Therefore, the flow field was in the transcritical condition. The isobaric-specific heat shows the peak at the pseudo-critical temperature. Most of the peak regions of the isobaric-specific heat were near the heated wall, while some peak regions extended in the mainstream direction. Fig. 12(c) shows the streamwise velocity with cross-stream velocity vectors superimposed. Secondary flows orthogonal to the streamwise velocity existed near the wall. The high-temperature region accompanied by low-speed streamwise velocity was transported by outward flow near the heated wall.
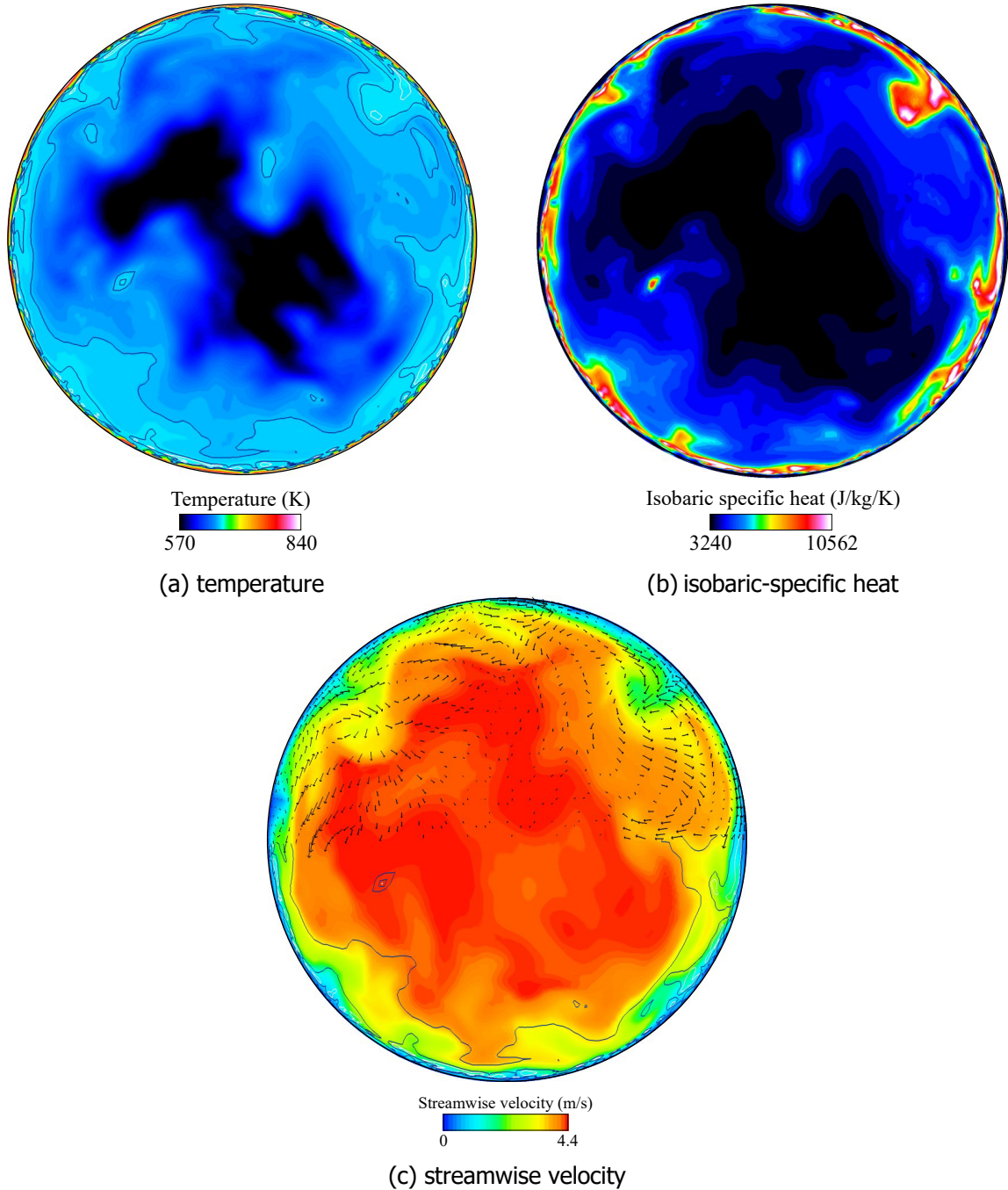
(a) temperature

(b) isobaric-specific heat

(c) streamwise velocity

Fig 12. Instantaneous snapshots in the cross-section at $z/D = 180$ with superimposed black ($c_p = 5000$) and white ($c_p = 10000$) contour lines at $G = 1.75$ g/s and $p = 2.0$ MPa.

Fig. 13 shows instantaneous snapshots of the wall-parallel plane for the temperature, density fluctuation, Favre-averaged streamwise velocity fluctuation, and Favre-averaged wall-normal velocity fluctuation at $r/D = 0.45$ under the computational conditions of $G = 1.75$ g/s and $p = 2.0$ MPa. The black contour lines in Fig. 13(a) indicate the high isobaric-specific heat region of $c_p > 4000$. Figs. 13(c, d) shows the high-speed ($u_z'' > 0$) and low-speed ($u_z'' < 0$) streaks near the heated wall. These streaks formed the streamwise-elongated structure, which typically exists in wall turbulence. The high-speed streaks corresponded to outward flows ($u_r'' > 0$) and transported the low-temperature ($T < T_{pc}$) liquid-like fluid toward the heated wall (note the area framed in white in Fig. 13(a)). The turbulent structure had the properties of $u_z'' > 0$, $u_r'' > 0$, and $\rho' > 0$, and corresponds to the sweep event. On the one hand, the low-speed streaks corresponded to inward flows ($u_r'' < 0$) and transported the high-temperature ($T > T_{pc}$) gas-like fluid toward the heated wall. The turbulent structure had the properties

of $u_z'' < 0$, $u_r'' < 0$, and $\rho' < 0$, which corresponds to the sweep event.
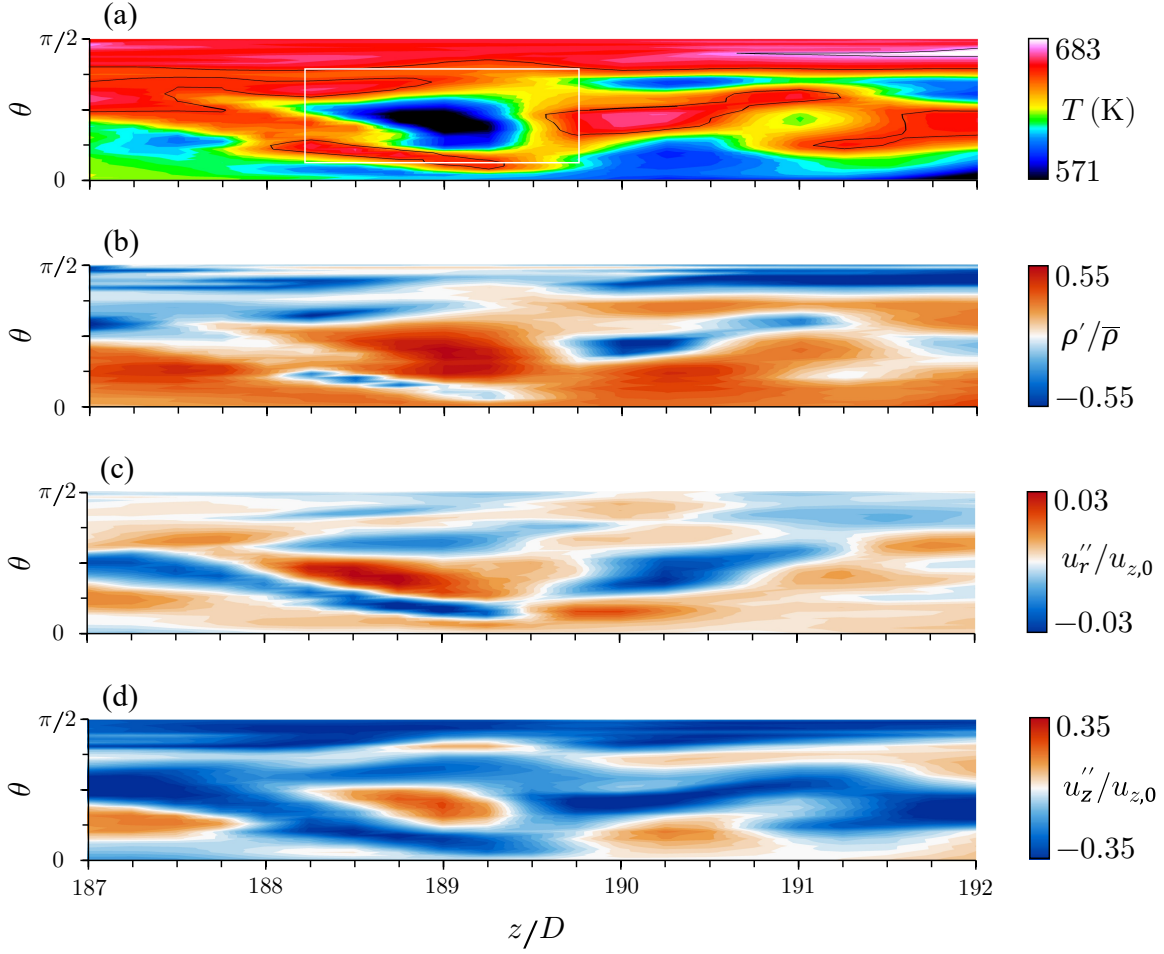

Fig 13. Instantaneous snapshots of the wall-parallel plane at $r/D = 0.45$ under the computational conditions of $G = 1.75$ g/s and $p = 2.0$ MPa.

Fig. 14 shows instantaneous snapshots of velocity fluctuations and turbulent mass fluxes in the cross section at $z/D = 195$ under the computational conditions of $G = 1.75$ g/s and $p = 2.0$ MPa. Fig. 14 demonstrates that high-speed and low-speed streaks correspond to outward and inward flows, respectively. Figs. 14(c, d) shows streamwise and radial turbulent mass fluxes. Here, there is a relationship between the turbulent mass flux and instantaneous Favre-averaged velocity fluctuation as follow:

$$u_i'' = u_i - \widetilde{u_i} = u_i' - \frac{\overline{\rho' u_i'}}{\overline{\rho}}. \tag{6}$$

Eq. (6) indicates that Favre-averaged velocity fluctuations are enhanced or reduced by the turbulent mass fluxes $\rho' u_i'$ related to the density fluctuation. In the present case, positive turbulent mass fluxes corresponded to both high-speed and low-speed streaks in most of the flow fields. Therefore, the turbulent mass fluxes reduced the sweep event ($u_z'' > 0$ and $u_r'' > 0$) and enhanced the ejection event ($u_z'' < 0$ and $u_r'' < 0$). The enhancement and reduction in Favre-averaged velocity fluctuations by the effect of density fluctuation were also demonstrated in the DNS of heated transcritical flat-plate turbulent boundary layers [22] and in the DNS of heated transcritical spatial-developing pipe flows [23]. The present study newly showed that the density fluctuation effect common in transcritical flows exhibited in the negative slope region of the hydrodynamic characteristic curves.
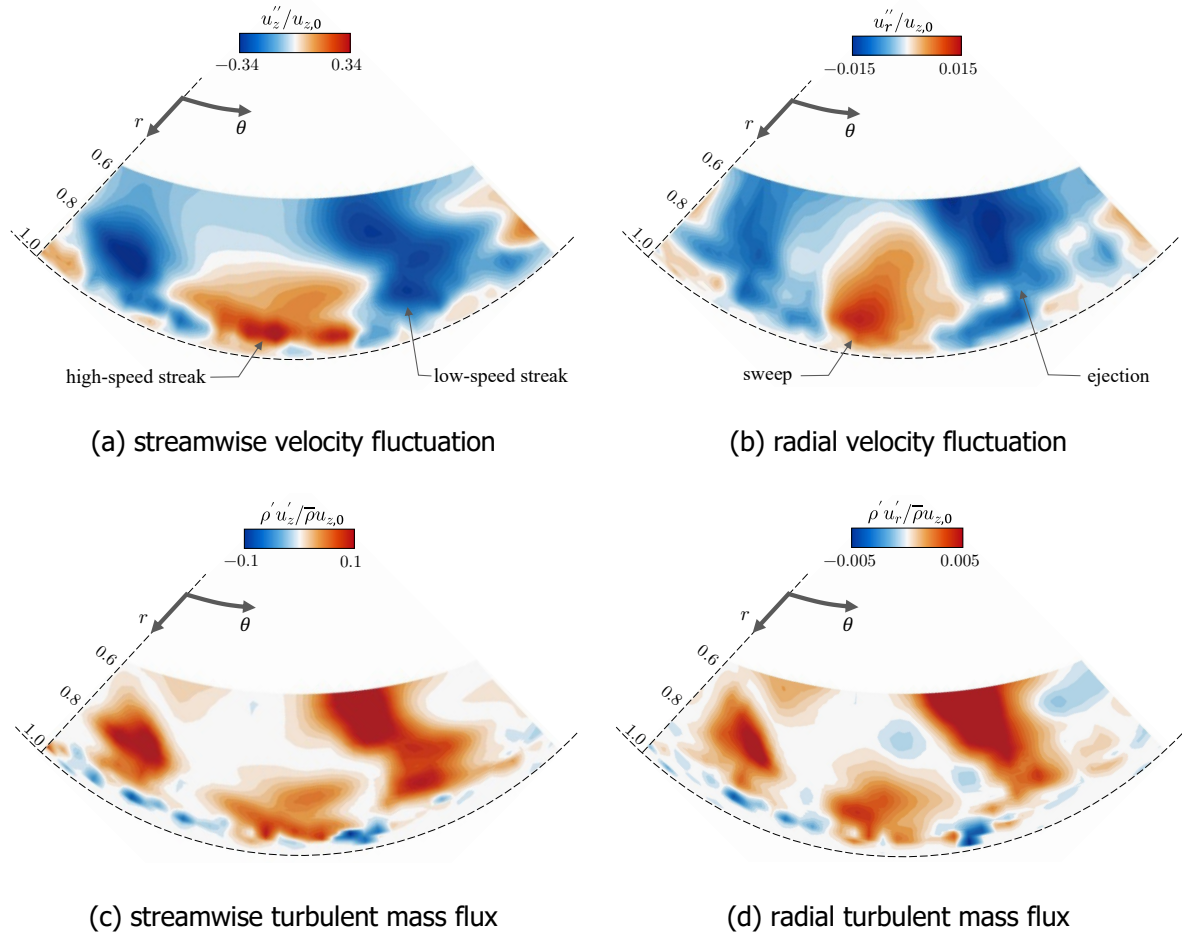
(a) streamwise velocity fluctuation

(b) radial velocity fluctuation

(c) streamwise turbulent mass flux

(d) radial turbulent mass flux

Fig 14. Instantaneous snapshots of Favre-averaged velocity fluctuations and turbulent mass fluxes in the cross-section at $z/D = 195$ under the computational conditions of $G = 1.75 \text{ g/s}$ and $p = 2.0 \text{ MPa}$.

Fig. 15 shows instantaneous snapshots of iso-surfaces of near-wall low-speed streaks at $p = 2 \text{ MPa}$ and $p = 6 \text{ MPa}$ under the mass flow rate condition of $G = 1.75 \text{ g/s}$. Three-dimensional turbulent structures, which are colored by the density fluctuation, at different three streamwise positions were visualized to investigate the spatial-developing flow. Arrows in Fig. 15 indicate inflows. At the inlet region ($0 < z/D < 20$), the density fluctuations were less for both pressure conditions $p = 2 \text{ MPa}$ and $p = 6 \text{ MPa}$ because the fluid was not heated sufficiently to cause a large density change. The fluid was gradually heated toward the outlet, and the fluid density was drastically changed when crossing the pseudo-critical temperature, resulting in density fluctuation appeared. Fig. 15 shows that the density fluctuation at $p = 2 \text{ MPa}$ is intensified compared with that at $p = 6 \text{ MPa}$. As shown in Fig. 4(b), the fluid density significantly changes approaching the critical pressure. In addition, the density change in the transcritical condition becomes abrupt, i.e., slight changes in temperature lead to large changes in density. As a result, large density fluctuations are induced under pressure conditions near the critical point. Inward flows accompanied by negative density fluctuations were observed at $p = 2 \text{ MPa}$. From Eq. (6), the ejection ($u_z'' < 0$ and $u_r'' < 0$) was intensified by negative density fluctuations associated with the pseudo-boiling. That is why the ejection at $p = 2 \text{ MPa}$ was gradually intensified toward the downstream. At $p = 6 \text{ MPa}$, there was little density fluctuation and no obvious development of the ejection in the streamwise direction compared with the case of $p = 2 \text{ MPa}$. The density fluctuation is highly dependent on pressure, and the effect significantly appeared in the outlet region ($180 < z/D < 200$) as a difference in discharge behavior.
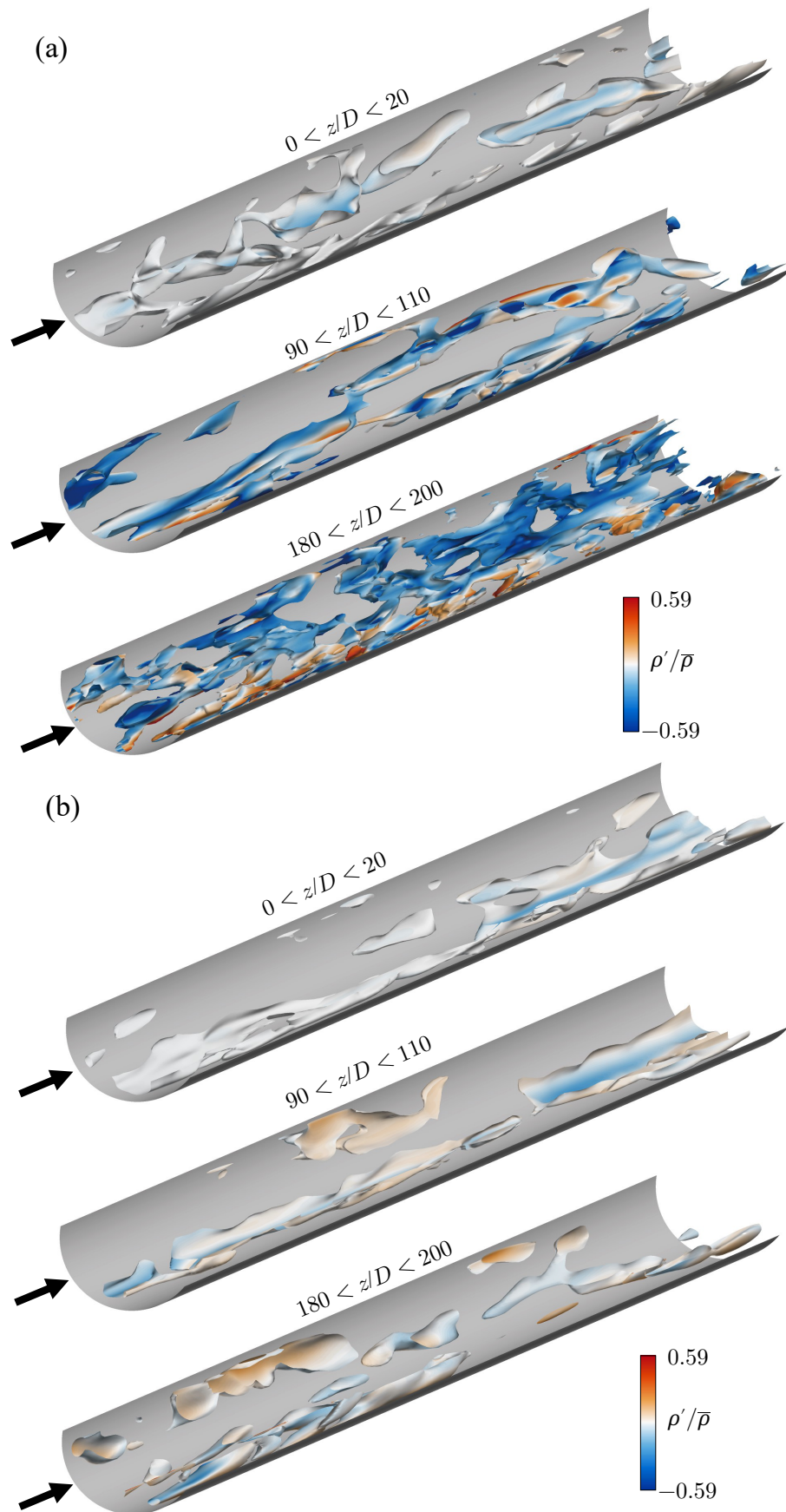
(a)

$0 < z/D < 20$

$90 < z/D < 110$

$180 < z/D < 200$

0.59

$\rho'/\overline{\rho}$

−0.59

(b)

$0 < z/D < 20$

$90 < z/D < 110$

$180 < z/D < 200$

0.59

$\rho'/\overline{\rho}$

−0.59

Fig 15. Instantaneous snapshots of iso-surfaces of ejection ($u_r'' = -0.01$) motions colored by density fluctuations at (a) $p = 2.0$ MPa and (b) $p = 6.0$ MPa under the mass flow rate condition of $G = 1.75$ g/s.

5. Conclusions

In the present study, we investigated the mechanisms behind the formation of the multi-valued hydrodynamic characteristic curves using the LES code. To validate the numerical method of LES, the simulated adiabatic friction factors in a horizontal circular tube were compared with theoretical value and previous correlation to evidence enough capability of predicting the pressure field. Eventually, the LES were conducted for n-dodecane flows in the horizontal heated circular tube at supercritical pressure. Hydrodynamic characteristic curves were obtained under different three supercritical pressure conditions of 2.0, 2.5, and 6.0 MPa. The hydrodynamic characteristic curve at $p = 2.0 \text{ MPa}$ and 2.5 MPa had negative slope regions, which suggests the possibility of Ledinegg instability. The pressure drop significantly increased with approaching the pseudocritical pressure. The enhancement of ejection motion associated with large density fluctuations at $p = 2.0 \text{ MPa}$ induced the negative radial velocity. The radial transport of the low-density fluid near the heated wall to the mainstream by vigorous ejection motion led to a decrease in bulk density and a significant flow acceleration. Eventually, it was clarified that the increase in acceleration pressure drop at $p = 2.0 \text{ MPa}$ caused the formation of a negative slope region in the hydrodynamic characteristic curve of the heated circular tube. In addition, the mechanisms of heat transfer enhancement/deterioration related to the intense ejection motion and the flow acceleration were elucidated by using the FIK identity for the Nusselt number. The present LES analyzed transcritical flows in the heated circular tube by visualizing flow properties, such as temperature and density profiles, and turbulence statistics. As a result of the visualization, the enhancement and reduction mechanism of Favre-averaged velocity fluctuations by the effect of density fluctuation were demonstrated in the transcritical flows corresponding with the negative slope region of the hydrodynamic characteristic curve.

References

1. M. Ledinegg, "Instability flow during natural forced circulation," Die Waerme, 61, (1938), 891–898.
2. S. Kakac, B. Bon, "A Review of two-phase flow dynamic instabilities in tube boiling systems," International Journal of Heat and Mass Transfer, 51, (2008), 399–433.
3. L.C. Ruspini, C.P. Marcel, A. Clausse, "Two-phase flow instabilities: A review," International Journal of Heat and Mass Transfer, 71, (2014), 521–548.
4. J.A. Boure, A.E. Bergles, L.S. Tong, "Review of two-phase flow instability," Nuclear Engineering and Design, 25, (1973), 165–192.
5. S. Tomioka, T. Hiraiwa, T. Saito, K. Kato, M. Kodera, K. Tani, "System analysis of a hydrocarbon-fueled RBCC engine applied to a TSTO launch vehicle," Transactions of the Japan Society for Aeronautical and Space Sciences, Aerospace Technology Japan, 12 (29) (2014) 91–99.
6. B. Hitch, M. Karpuk, Experimental investigation of heat transfer and flow instabilities in supercritical fuels, AIAA 3043 (1997).
7. H. Wang, J. Zhou, Y. Pan, N. Wang, "Experimental investigation on the onset of thermo-acoustic instability of supercritical hydrocarbon fuel flowing in a small-scale channel," Acta Astronautica, 117, (2015), 296–304.
8. W. Ambrosini, "On the analogies in the dynamic behaviour of heated channels with boiling and supercritical fluids," Nuclear Engineering and Design, 237, (2007), 1164–1174.
9. W. Zhou, B. Yu, J. Qin, D. Yu, "Mechanism and influencing factors analysis of flowing instability of supercritical endothermic hydrocarbon fuel within a small-scale channel," Applied Thermal Engineering, 71, (2014), 34–42.
10. Z. Yang, Y. Shan, B. Zhang, Y. Liu, "Hydrodynamic characteristics of cyclohexane in a horizontal mini-tube at trans- and supercritical pressures," Applied Thermal Engineering, 129, (2018), 62–69.
11. J.M. Weiss, W.A. Smith, "Preconditioning applied to variable and constant density flows," AIAA Journal, 33, (1995), 2050–2056.
12. N. Alkishriwi, M. Meinke, W. Schroder, "A large-eddy simulation method for low Mach number flows using preconditioning and multigrid," Computers & Fluids, 35, (2006), 1126–1136.
13. P. Renze, W. Schroder, M. Meinke, "Large-eddy simulation of film cooling flows at density gradients," International Journal of Heat and Fluid Flow, 29, (2008), 18–34.
14. S. Yang, X. Wang, V. Yang, W. Sun, H. Huo, "Comparison of flamelet/progress-variable and finite-rate chemistry LES models in a preconditioning scheme," 55th AIAA Aerospace Sciences Meeting (AIAA 2017-0605).

15. S. Yamamoto, "Preconditioning method for condensate fluid and solid coupling problems in general curvilinear coordinates," Journal of Computational Physics, 207, (2005), 240–260.

16. Y. Jiang, C.-W. Shu, and M. Zhang, "An Alternative Formulation of Finite Difference Weighted ENO Schemes with Lax--Wendroff Time Discretization for Conservation Laws," SIAM Journal on Scientific Computing, 35, (2013), A1137–A1160.

17. S. Yatsuyanagi, T. Furusawa, S. Yamamoto, "Double-flux model for supercritical multicomponent flows at low Mach numbers with preconditioning method," Journal of Computational Physics, 458, (2022), 111091.

18. S.K. Lele "Compact finite difference schemes with spectral-like resolution," Journal of Computational Physics, 103, (1992),16–42.

19. E.W. Lemmon and M.L. Huber, "Thermodynamic properties of n-dodecane," Energy & Fuels, 18(4), (2004), 960–967.

20. M.L. Huber, A. Laesecke, R.A. Perkins, "Transport properties of n-dodecane," Energy & Fuels, 18, (2004), 968–975.

21. E.W. Lemmon, I.H. Bell, M.L. Huber, M.O. McLinden, NIST Standard Reference Database 23: Reference Fluid Thermodynamic and Transport Properties-REFPROP, Version 10.0, National Institute of Standards and Technology, 2018.

22. S. Kawai, "Heated transcritical and unheated non-transcritical turbulent boundary layers at supercritical pressures," Journal of Fluid Mechanics, 865, (2019), 563-601.

23. J. Liu, P. Zhao, M. Lei, S. Yang, H. Nemati, "Numerical investigation of spatial-developing turbulent heat transfer in forced convections at different supercritical pressures," International Journal of Heat and Mass Transfer, 159, (2020), 120128.

24. K. Fukagata, K. Iwamoto, N. Kasagi, "Contribution of Reynolds stress distribution to the skin friction in wall-bounded flows," Physics of Fluids, 14, (2002), L73–L76.

25. K. Fukagata, N. Kasagi, "Drag reduction in turbulent pipe flow with feedback control applied partially to wall," International Journal of Heat and Fluid Flow, 24, (2003), 480–490.

26. T. Gomez, V. Flutet, P. Sagaut, "Contribution of Reynolds stress distribution to the skin friction in compressible turbulent channel flows," Physical Review E, 79, (2009), 035301.

27. Y. Kametani, K. Fukagata, "Direct numerical simulation of spatially developing turbulent boundary layers with uniform blowing or suction," Journal of Fluid Mechanics, 681, (2011), 154–172.

28. J. Lee, S.Y. Jung, H.J. Sung, T.A. Zaki, "Effect of wall heating on turbulent boundary layers with temperature-dependent viscosity," Journal of Fluid Mechanics, 726, (2013), 196–225.

29. P. Zhao, J. Liu, Z. Ge, Y. Li, N. Zhao, Y. Wan, "Direct numerical simulation of strongly heated air flows in a vertical pipe using a thermophysical property table," International Journal of Heat and Mass Transfer, 124, (2018), 1181–1197.

30. P. Zhao, T. Wan, Y. Jin, Z. Chen, Y. Li, and C. Peng, "Direct numerical simulation analysis of heat transfer deterioration of supercritical fluids in a vertical tube at a high ratio of heat flux to mass flowrate," Physics of Fluids, 33, (2021), 055114.